Volume 3 | Number 15 | 21 April 2015 | Pages 7669–8216

Journal of Materials Chemistry A

Materials for energy and sustainability

www.rsc.org/MaterialsA

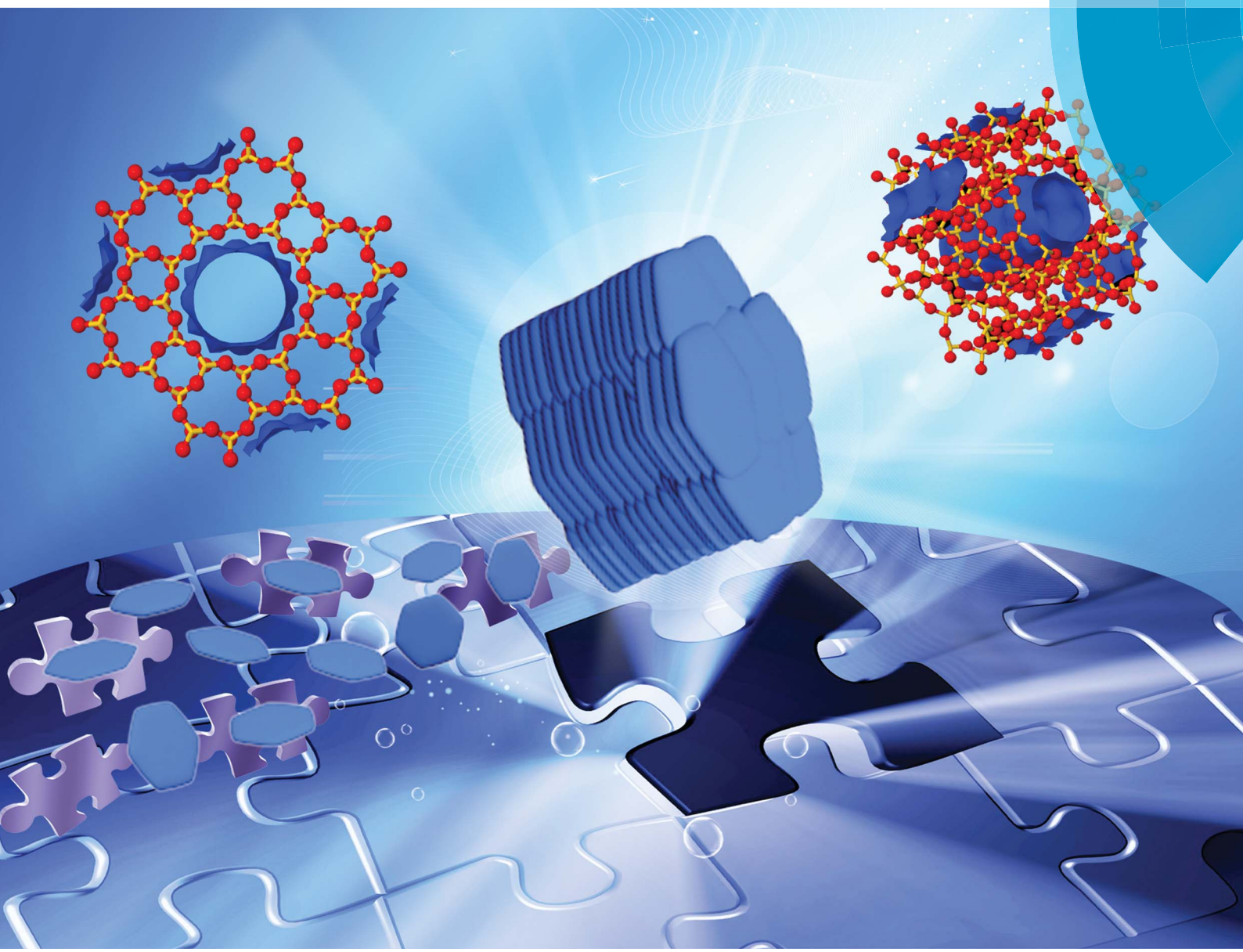

ISSN 2050-7488

ROYAL SOCIETY OF CHEMISTRY

PAPER

Zhongmin Liu *et al.*

In situ growth and assembly of microporous aluminophosphate nanosheets into ordered architectures at low temperature and their enhanced catalytic performance

Journal of Materials Chemistry A

PAPER

View Article Online
View Journal | View Issue

Cite this: J. Mater. Chem. A, 2015, 3, 7741

In situ growth and assembly of microporous aluminophosphate nanosheets into ordered architectures at low temperature and their enhanced catalytic performance†

Beibei Gao,[ab] Peng Tian,[a] Mingrun Li,[c] Miao Yang,[a] Yuyan Qiao,[ab] Linying Wang,[a] Shutao Xu[a] and Zhongmin Liu*[ac]

Received 3rd February 2015
Accepted 18th February 2015

DOI: 10.1039/c5ta00888c

www.rsc.org/MaterialsA

A low-temperature strategy to fabricate hierarchical aluminophosphate-based molecular sieves has been developed without the assistance of surfactants. The facile synthesis results in cylinder-like SAPO-5 (AFI) composed of oriented attached nanosheets with a thickness of 40–100 nm. The main exposed surface of the nanosheets is revealed by the SAED pattern to be the {001} plane, implying a short path for molecular diffusion in the one-dimensional 12-membered ring channel. Investigation on the crystallization process demonstrates that low temperature retards the crystal growth along the *c*-direction in SAPO-5 and the ordered architecture forms *via* a nanosheet formation and oriented attachment process. The aggregated morphology of SAPO-5 is template-dependent, which may be modified/changed by varying the template in the system. The low-temperature strategy is also successfully extended to the preparation of metal-containing aluminophosphate molecular sieves. The obtained MeAPO-5 (Me = Co, Mn, and Cr) and a novel CHA/AEI intergrowth CoAPO molecular sieve also possess hierarchical structures with nanosheet-assembled morphology. Remarkably, the present self-assembled AFI crystals exhibit an obvious improvement in catalytic reactions. This facile method provides a new way for the long-range organization of nanosized building blocks to fabricate hierarchical nanostructures.

Introduction

The fabrication of inorganic hierarchical nanostructures, which are assembled from nanoscale building blocks, has attracted considerable attention in materials chemistry due to their distinct properties for specific applications.[1–8] Over the past few years, much effort has been devoted to the development of strategies for the long-range organization and assembly of nanostructured phases. Conventionally, highly ordered inorganic frameworks are synthesized through preparing building blocks such as nanosized particles generated either beforehand or *in situ*, followed by further self-assembly processing such as programmed recognition,[9] solvent evaporation,[10] molecular cross-linking[11] or surfactant-assistance.[12–15] Research on hierarchical structures facilitates a better understanding of the "bottom-up" approaches and provides opportunities for optimized properties and applications of materials.[5,16,17] So far, many kinds of compound materials, such as metals,[18–20] metal oxides/hydroxides,[21–24] graphene oxide[25] and aerogels,[26] have been synthesized with controlled hierarchical structures.

Zeolites are a family of microporous crystalline materials with uniform and molecular-sized pores and have been widely used as heterogeneous catalysts in the petrochemistry and fine chemical industries.[27] However, the sole molecular-sized micropores limit the catalytic performance of the zeolites because of the restricted intracrystalline transport, which greatly hinders their industrial applications.[28] Therefore, the synthesis of nanocrystals or construction of hierarchical zeolite structures has attracted increasing attention and promises to improve the catalysis efficiency of zeolites.[29,30] Currently, the most attractive method to prepare hierarchical zeolites is a template-assisted assembly process, including soft templates and hard templates, which could afford ordered mesoporous materials in a range of length scales.[11,31–38] To effectively avoid the introduction of secondary templates and simplify the synthesis procedure, direct methods in which synthesis and

[a]National Engineering Laboratory for Methanol to Olefins, Dalian National Laboratory for Clean Energy, Dalian Institute of Chemical Physics, Chinese Academy of Sciences, Dalian 116023, P. R. China. E-mail: liuzm@dicp.ac.cn; Fax: +86-411-84379289; Tel: +86-411-84379998

[b]University of Chinese Academy of Sciences, Beijing 100049, P. R. China

[c]State Key Laboratory of Catalysis, Dalian Institute of Chemical Physics, Chinese Academy of Sciences, Dalian 116023, P. R. China

† Electronic supplementary information (ESI) available: Additional XRD patterns, SEM images, DR UV-Vis spectra, NH_3-TPD curves and porous properties of samples. See DOI: 10.1039/c5ta00888c

self-assembly are coupled *in situ* to yield highly ordered structures have to be developed. There are, however, only a few examples reported where those nanoblock-built microarchitectures could be prepared in a controllable manner without a secondary template.[38–41] Ren *et al.* successfully fabricated plate-like micro-sized MOR and Fe-MOR zeolite crystals assembled from highly uniform nano-rods by an organotemplate-free method during one-pot crystallization in the presence of a MOR seed solution.[39] They found that the seed solution rich in 4-membered rings played a critical role in the formation of a unique structure. Fang *et al.* reported that mesoporous zeolites could be synthesized without a secondary template through self-assembly of *in situ* formed nanocrystals by employing a concentrated synthesis gel to enhance the zeolite nucleation rate.[40] The as-synthesized mesoporous aggregates have single-crystal-like morphology with high hydrothermal stability and large mesoporosity. Likewise, a hierarchical self-sustaining macroscopic zeolite beta was synthesized with TEAOH as the template by steam-assisted conversion.[41] The mesoporosity is introduced by the assembly of the 20 nm crystalline domains of zeolite beta whose growth is arrested by the dense packing in the dry gel. Moreover, the discovery of novel bifunctional templates, such as multivalent surfactants and cationic polymers, also brings opportunities for the synthesis of mesoporous zeolites without a secondary template. Stable single-unit-cell ZSM-5 nanosheets and mesoporous single-crystalline beta have been achieved by this strategy.[42,43]

It is well acknowledged that the crystallization temperature has a great influence on the zeolite nucleation and growth rate, which may alter the reaction intermediate/process, and lead to different crystal phases, morphologies, and sizes.[44–48] Synthesis at lower temperature tends to reduce the crystallization rate and achieve nanosized zeolites.[44,47,48] However, although the low-temperature syntheses have been studied by several groups,[44,48–51] very few cases by simply employing low temperature to build ordered hierarchical structures have been achieved. In this paper, we report a facile and surfactant-free approach to synthesize SAPO-5 molecular sieve nanosheet assemblies by conducting crystallization at a lower temperature (120 °C). The formation process of the ordered structures is investigated in detail and a growth model is proposed. The possibility to synthesize metalaluminophosphate molecular sieves at low temperature is also explored and all the samples obtained show aggregated morphology assembled by nanosheets. The self-assemblies display excellent catalytic performance as compared with the conventional samples.

Experimental section

Synthesis of samples

Organic templates used in the synthesis were triethylamine (TEA, 99 wt%, Tianjin Damao Chemical Reagent Co.), dimethylethanolamine (99 wt%, Tianjin Damao Chemical Reagent Co.), hexamethyleneimine (99 wt%, Tianjin Damao Chemical Reagent Co.), choline chloride (98 wt%, Sinopharm Chemical Reagent Co.), tripropylamine (TPA, 99 wt%, Shanghai Aladdin industrial Co.), tetraethylammonium hydroxide (TEAOH, 35 wt%, Zhenjiang Runjing Chemical Co.), and tetraethylammonium bromide (TEABr, 99 wt%, Shanghai Annaiji Chemical Reagent Co.). Pseudoboehmite (67.5 wt%, Shandong Chemical Co.), phosphoric acid (85.0 wt%, Sichuan Xianfeng Chemical Co.), and silica sol (31.0 wt%, Shenyang Chemical Co.) were used as inorganic resources. All the chemicals were used without further purification.

The typical gel ratio for SAPO-5 nanosheet assemblies was $1.5TEA : 0.8Al_2O_3 : 1.0P_2O_5 : 0.5SiO_2 : 50H_2O$. The synthesis was carried out as follows: 3.02 g pseudoboehmite was added to a solution containing 5.76 g of phosphoric acid and 17.60 g of water under stirring. The mixture was stirred at room temperature for 5 h, and then 2.43 g silica sol was added into the mixture and stirred for 30 min. After further addition of organic amine, the resulting mixture was transferred into a 50 mL autoclave, which was heated to 120 °C within 60 min and kept at this temperature for 24 h under rotation. After the crystallization, the solid product was recovered by filtration, washed with distilled water, and dried in air. The product yield based on the calcined oxides is about 32.7 wt%.

MeAPO-5 nanosheet assemblies were hydrothermally prepared using TEA as the organic template. The metal sources used were manganese acetate tetrahydrate, cobalt acetate tetrahydrate, and chromium nitrate nonahydrate, respectively, for MnAPO-5, CoAPO-5, and CrAPO-5. The molar ratios of the reaction mixtures were $1.5TEA : 0.5Al_2O_3 : 1.0P_2O_5 : 0.04MeO_x : 50H_2O$ for the synthesis of MnAPO-5 and CoAPO-5 and $1.5TEA : 0.5Al_2O_3 : 1.0P_2O_5 : 0.06MeO_x : 50H_2O$ for CrAPO-5. For the synthesis of MnAPO-5 and CoAPO-5, a small amount of $AlPO_4$-5 was used as seeds (10 wt% in relation to the sum of SiO_2, Al_2O_3, and P_2O_5 contents in the initial mixtures). In a typical procedure, 1.89 g pseudoboehmite was mixed with a solution containing 5.76 g of phosphoric acid and 14.69 g of water under stirring. Then, 0.25 g of cobalt acetate tetrahydrate dissolved in 5 mL of H_2O was combined with this mixture and stirred for 30 min. 0.48 g AlPO-5 seeds were then added to the gel, followed by dropwise addition of 3.80 g of TEA. The final mixture was stirred for 2 h before being transferred to an autoclave for crystallization at 120 °C for 48 h. After crystallization, the product was separated from the mother liquor, washed with water, and dried at 100 °C overnight.

The CHA/AEI intergrowth CoAPO molecular sieve was hydrothermally synthesized with a gel composition of $1.0TEA : 0.5TEABr : 0.8Al_2O_3 : 1.0P_2O_5 : 0.06CoO : 50H_2O$. The detailed synthesis procedure and crystallization conditions were similar to those of MeAPO-5 nanosheet assemblies. The product yield based on the calcined oxides is about 80 wt%.

Conventional SAPO-5-C and MnAPO-5-C were hydrothermally synthesized with gel compositions of $1.2TEA : 1.0Al_2O_3 : 1.0P_2O_5 : 0.3SiO_2 : 50H_2O$ (170 °C, 24 h) and $1.2TEA : 1.0Al_2O_3 : 1.0P_2O_5 : 0.06MnO : 50H_2O$ (200 °C, 48 h), respectively.

Characterization

The crystal morphology and structure were observed by scanning electron microscopy (SEM, Hitachi SU8020), transmission

electron microscopy (TEM, Philips-FEI Tecnai F30) and selected-area electron diffraction (SAED). The powder XRD pattern was recorded to determine the crystalline phase on a PANalytical X'Pert PRO X-ray diffractometer with Cu-Kα radiation (λ = 1.54059 Å), operating at 40 kV and 40 mA. The chemical compositions of the solid samples were determined with a Philips Magix-601 X-ray fluorescence (XRF) spectrometer. Textural properties of the calcined samples were measured by N_2 adsorption at −196 °C on a Micromeritics ASAP 2020 analyzer. The total surface area was calculated based on the BET equation. The micropore volume and micropore surface area were evaluated by using the *t*-plot method.

The acid properties of selected SAPO-5 samples were determined by temperature-programmed desorption of ammonia (NH_3-TPD, Micromeritics Autochem II 2920 device). The samples (200 mg) were outgassed in a He flow at 600 °C for 60 min. And then the samples were cooled down to 100 °C and subjected to a flow of NH_3/He for 30 min to saturate the sample with NH_3. Subsequently, the samples were purged with a He flow to remove the weakly adsorbed NH_3 molecules. The measurement of the desorbed NH_3 was performed from 100 to 650 °C at a heating rate of 10 °C min^{-1} under a He flow (20 mL min^{-1}). Diffuse reflectance UV-Vis spectra in the range of 200–800 nm were recorded against a $BaSO_4$ reference standard on a VARIAN Cary-5000 UV-Vis-NIR spectrophotometer equipped with an integration sphere. ^{13}C CP/MAS NMR experiments were performed on a Bruker Avance III 600 spectrometer equipped with a 14.1 T wide-bore magnet and 4 mm MAS probe with a spinning rate of 12 kHz. The spectrum was recorded at 150.9 MHz with a contact time of 3 ms and a recycle delay of 2 s.

Catalytic tests

Before the catalytic use, all samples were calcined in air by slowly raising the temperature to 600 °C and holding at this temperature for 4 h to remove the organic templates.

Alkylation of benzene (99.5%) with benzyl alcohol (98.0%) was performed in a batch reactor (100 mL, PARR autoclaves 4560). The reaction mixture for benzene alkylation contained 29.8 g benzene, 0.52 g benzyl alcohol, and 0.31 g catalyst. The reactor was purged with nitrogen and a permanent pressure of 3.4–3.6 MPa was maintained during the reaction to keep the reactants in the liquid phase at a reaction temperature of 160 °C. The mixture was stirred throughout the run. The products were analyzed on an Agilent GC 7890 gas chromatograph equipped with an FID detector and HP-5 MS capillary column.

Cyclohexane oxidation with oxygen was performed in a batch reactor (100 mL, PARR autoclaves 4560). Typically, the catalyst (0.019 mmol Mn), 23.5 mL cyclohexane, and 0.07 mL of cumene hydroperoxide (CHP, initiator) were added to the reactor. Oxygen was then charged into the reactor to 1.4 MPa. The mixture was heated to 130 °C and maintained at this temperature for 3 h under stirring. After the reaction, the liquid products were separated by centrifugation and analyzed using a GC-MS (Agilent 7890A/5975C) equipped with a HP-5 MS capillary column. As cyclohexyl hydroperoxide (CHHP) partially decomposed upon injection, its concentration was estimated by double analyses, before and after reducing CHHP to cyclohexanol with Ph_3P.

Results and discussion

Synthesis and crystallization process of SAPO-5 nanosheet assemblies

A SAPO-5 nanosheet assembly (designated as SAPO-5-NS1) was synthesized from a silicoaluminophosphate gel with a typical molar composition of 1.5TEA : 0.8Al_2O_3 : 1.0P_2O_5 : 0.5SiO_2 : 50H_2O at 120 °C for 24 h. The XRD pattern (Fig. S1†) shows characteristic peaks of the AFI-type molecular sieve, suggesting the formation of SAPO-5 crystals. Fig. 1a shows a low magnification SEM image of SAPO-5-NS1, which has a relatively uniform cylinder-like morphology with particle sizes of about 7 × 7 μm. Further magnification in Fig. 1b reveals that these particles have hierarchical structures constructed through oriented attachment of nanosheet crystals. The thickness of the nanosheets is about 80 nm and they stack into multilayers in a parallel fashion.

TEM and selected area electron diffraction (SAED) were employed to determine the crystal growth behavior of SAPO-5-NS1. Fig. 1c presents the TEM micrograph of a SAPO-5-NS1 particle from the top view of the cylinder. Overlapped nanosheets could be observed in the outer fringe of the cylinder and the angles in the nanosheets are clearly close to 120°, revealing the hexagonal morphology of a single nanosheet. An enlarged image of the selected portion in Fig. 1c is

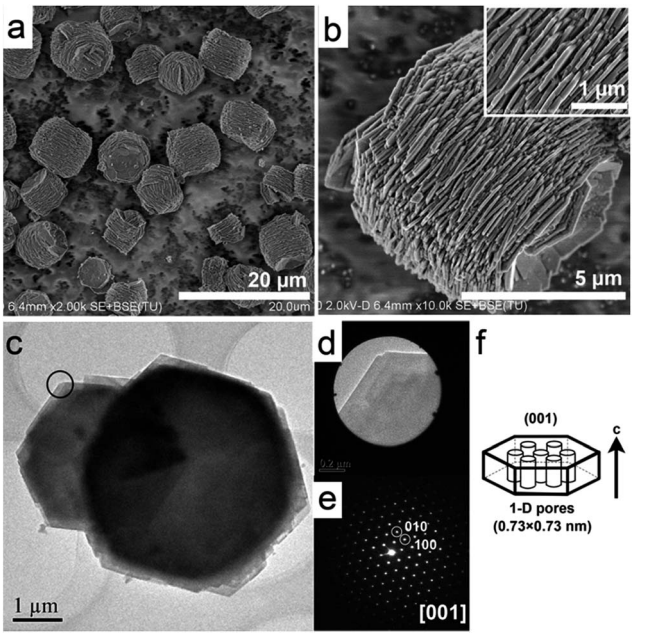

Fig. 1 SEM and TEM images of the product SAPO-5-NS1: (a) low magnification SEM image; (b) high magnification SEM image to show the ordered structure of SAPO-5-NS1 (inset: further magnified micrograph); (c) TEM image of the SAPO-5-NS1 particle; (d) enlarged TEM image of the portion labeled by a circle; (e) the corresponding SAED pattern; (f) a schematic to illustrate the one-dimensional channel system running along the *c*-axis in SAPO-5.

displayed in Fig. 1d and the corresponding SAED pattern of this part is shown in Fig. 1e, which exhibits a hexagonal symmetry and can be indexed to the {001} crystal plane according to the AFI-type zeolite structure. This is also consistent with the angle of 120° in the nanosheets, indicating that the hierarchical cylinder-like SAPO-5-NS1 is assembled by SAPO-5 nanosheets along the [001] direction. Given that the AFI framework has a straight one-dimensional channel system running along the *c* crystallographic direction (Fig. 1f), this morphology would be favorable for catalytic applications due to the shortened diffusion path, which could reduce the diffusional limitation in the catalytic reactions.

Fig. 2 illustrates the nitrogen adsorption–desorption isotherms of SAPO-5-NS1, which shows a typical type IV isotherm with a hysteresis loop in the P/P_0 range of 0.4–0.9, revealing the existence of mesopores which probably root in the void space formed by the self-assembly of adjacent nanosheets. From the corresponding BJH pore size distribution curve calculated from the adsorption branch (inset in Fig. 2), it can be seen that the pore size distribution is relatively uniform, and the dominant pore diameter is about 12 nm. Herein, the desorption branch is avoided to be used for the mesopore size calculation due to the small hysteresis loop at $P/P_0 = 0.45$, which might yield false mesopores of 4 nm caused by the Tensile Strength Effect (TSE).[52] In comparison with the conventional SAPO-5-C (SEM image is shown in Fig. S4†), SAPO-5-NS1 exhibits a larger external surface area and higher mesopore volume (Table 1).

Generally, AFI crystals have a preferential growth along the *c*-direction with a high aspect ratio (*c*-axis/*a*-axis).[53] To elucidate the crucial parameters for the formation of the nanosheet-built microstructure of SAPO-5-NS1, syntheses with a more reactive silicon source or without silicon in the initial gel were carried out, considering that the introduction of silicon or metal is often found to change the growth habit and lead to the formation of a plate-like morphology.[54,55] Fig. 3a and b illustrate the SEM images of the products, which show similar morphologies to that of SAPO-5NS1. The thickness of the nanosheets in the sample synthesized without silicon is only about 40 nm, whereas active tetraethyl orthosilicate as the silicon source leads to a slight increase in the thickness. It

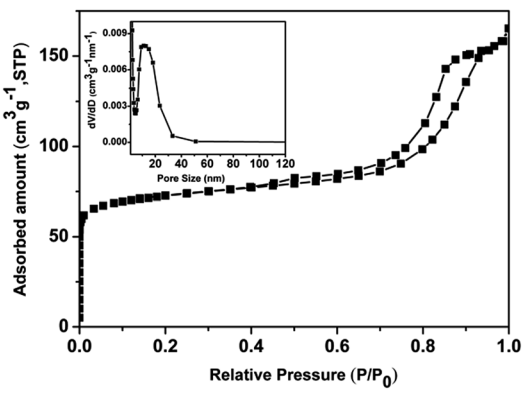

Fig. 2 N_2 adsorption–desorption isotherms of SAPO-5-NS1. The inset is the BJH pore size distribution calculated from the adsorption branch.

Table 1 The textural properties of the samples

Sample	Surface area ($m^2\ g^{-1}$)		Pore volume ($cm^3\ g^{-1}$)	
	S_{total}[a]	S_{exter}[b]	V_{micro}[c]	V_{meso}[d]
SAPO-5-NS1	272	79	0.09	0.16
SAPO-5-NS2	282	68	0.10	0.20
CoAPO-5-NS	348	65	0.13	0.10
MnAPO-5-NS	270	57	0.10	0.09
CrAPO-5-NS	264	86	0.08	0.20
DNL-7-Co	544	49	0.23	0.18
SAPO-5-C	300	40	0.12	0.05
MnAPO-5-C	286	32	0.12	0.02

[a] BET surface area. [b] *t*-plot external surface area. [c] *t*-plot micropore volume. [d] $V_{meso} = V_{total} - V_{micro}$, *V* total is evaluated at $P/P_0 = 0.99$.

implies that the addition of a silicon source is not critical to the formation of a hierarchical structure in the present system. Furthermore, control experiments at higher crystallization temperatures were performed to investigate the effect of crystallization temperature on the crystal growth habit. The SEM images of the samples are displayed in Fig. 3c and d. It can be seen that SAPO-5 obtained at 160 °C shows a hexagonal morphology with a rough external surface, which is in fact assembled by crystals with a *c*-axis length of ~1 μm. No nanosheets or their assembly could be found in the sample, which suggests the enhanced growth rate of the SAPO-5 crystal along the *c*-direction. Further increasing the crystallization temperature to 200 °C, hexagonal prism-like crystals with smooth surface are observed. The average aspect ratio of the crystals is higher than 1, indicating that the *c*-axis became the favored growth direction. From the above results, it is clear that the crystal growth behavior of SAPO-5 under the investigated conditions is rather sensitive to the temperature.

In order to understand the assembly mechanism of the SAPO-NS1, an investigation throughout the duration of the growing process was made by XRD and SEM. As shown in Fig. 4a, at the early stage (6 h), the sample is composed of irregular nanoparticle aggregates. The XRD pattern (Fig. 5) shows only weak broad peaks of pseudoboehmite, indicating an amorphous nature of the product. With further hydrothermal reaction for 11 h, a weak peak at 7.4° indexed to SAPO-5 could be observed. The corresponding SEM images (Fig. 4b and c) reveal that a small amount of round nanosheets and their aggregates crystallize from the amorphous gel, showing that the formation of the primary nanosheets and their quick aggregation take place meanwhile in the system. However, the aggregates are loosely organized and less ordered at the moment. As the reaction proceeds (14 h), the crystallinity of the solid product increases and the aggregates grow larger and are ordered at the expense of amorphous nanoparticles. Newly formed individual nanosheets can also be observed in the system. Besides, it should be noted that the obtained assembly may intercross with each other to form irregular morphologies. Further prolonging the crystallization to 24 h, the XRD peak intensities arising from SAPO-5 become sharp and strong and the broad peaks ascribed

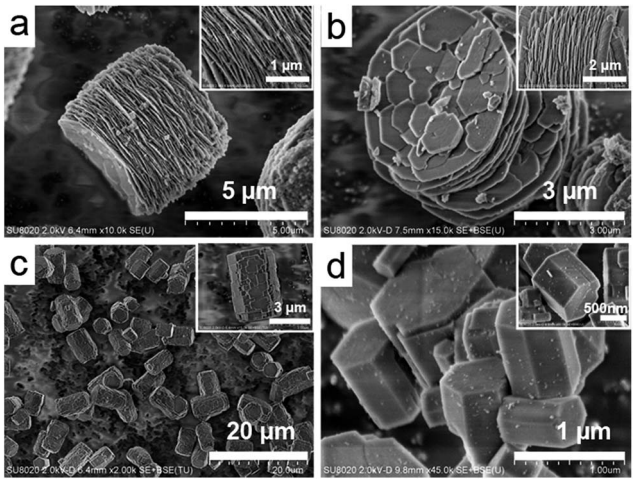

Fig. 3 SEM images of the samples: (a) AlPO-5-NS synthesized without silica; (b) SAPO-5-NS prepared with TEOS as the silicon source; (c) SAPO-5 prepared at 160 °C; (d) SAPO-5 prepared at 200 °C. The synthetic gels of (a–d) are the same as that of SAPO-5-NS1 except no Si source for (a).

to amorphous materials disappear completely. From the SEM image (Fig. 4f), it is clear that no amorphous nanoparticles exist and the obtained self-assembly consists entirely of the cylinder-like microstructures. Moreover, the edges of the round nanosheets grow into a clear hexagon, suggesting the gradual evolution of nanosheets even after their self-assembly.

Based on the above results, the formation mechanism of the SAPO-5-NS1 is proposed and depicted in Scheme 1. At the early stage of the crystallization, few round nanosheets with exposed {001} planes crystallize from the amorphous mixture and an oriented-attachment process (self-similar assembly), which could substantially reduce the surface energy, takes place. Afterwards, the aggregates grow larger and hierarchical structures appear. It is also easy for the formed aggregates to attach with each other in a random manner and generate larger intergrowth structures. Eventually, no amorphous nanoparticles and single nanosheet exist in the solid and the aggregated round nanosheets evolve with clear cut hexagonal edges. In addition, crystallographic fusion of the {001} faces in the center of the cylinders occurs as deduced from their slightly concave structures. However, the excessive fusion of the nanosheets might be suppressed by the higher activation energy for crystal growth at the low temperature and thus prevents the mesocrystal to transform into a single crystal. The present results suggest that the formation of the SAPO-5-NS1 architecture follows a non-classical crystallization pathway.[56]

During the synthesis, we noticed that SAPO-5 nanosheets assembled in a much less compact manner (designated as SAPO-5-NS2, Fig. 6a) could be obtained from a SAPO gel with the addition of TEABr (molar composition: 0.5TEABr/1.5TEA/$0.5Al_2O_3$/$1.0P_2O_5$/$0.5SiO_2$/$50H_2O$, 120 °C, 48 h). Moreover, the yield of this system (72.2%) could be greatly improved as compared to that of the single TEA template system (32.7%). As it has been reported that the adsorption of the quaternary ammonium ions to a certain plane can influence the

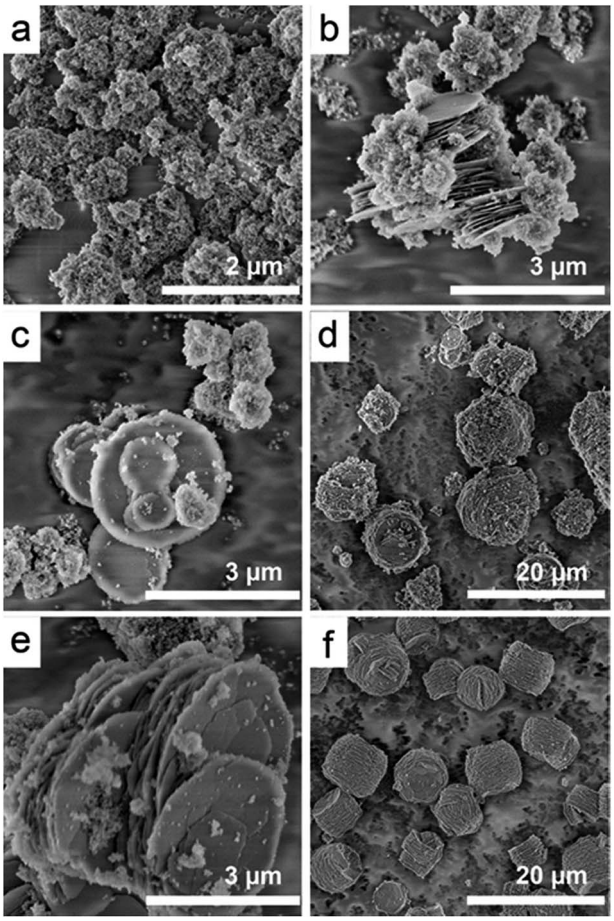

Fig. 4 SEM images of the products with different crystallization times: (a) 6 h; (b and c) 11 h; (d and e) 14 h; (f) 24 h.

morphology of the synthesized crystals,[57,58] we speculate that TEA^+ may preferentially adsorb onto the exposed {001} planes to reduce the surface energy of the nanosheets and thus lead to a loose assembly. In fact, when increasing the ratio of TEABr/TEA to 1/1.5, dispersible SAPO-5 nanosheets (Fig. 6b) could be obtained, which further confirmed our speculation. The N_2 physisorption results of sample SAPO-5-NS2 are given in Table

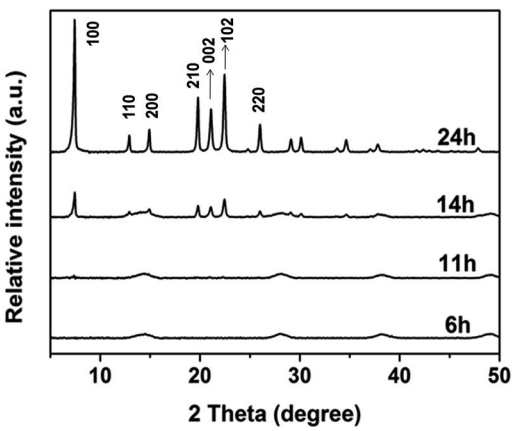

Fig. 5 XRD patterns of the products with different crystallization times.

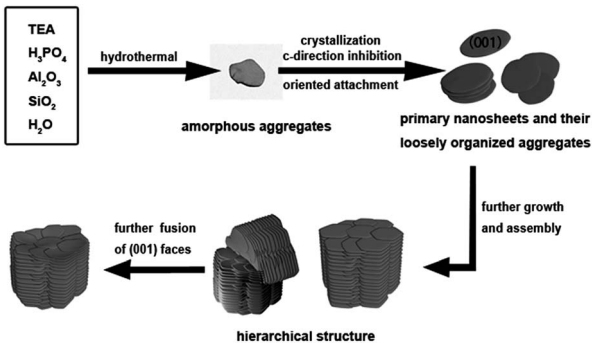

Scheme 1 Schematic illustration of the proposed low-temperature crystal growth route of SAPO-5-NS1.

1. The mesopore volume and external surface area are 0.20 $cm^3\ g^{-1}$ and 68 $m^2\ g^{-1}$ respectively, which are higher than those of conventional SAPO-5-C. Besides, in agreement with its loose stack, the mesopore volume of SAPO-5-NS2 is larger than that of SAPO-5-NS1, which would provide more capacious interspaces and thus offer more opportunities for the diffusion and mass transportation of molecules in the catalytic reactions.

Synthesis of SAPO-5 with other templates at low temperature

To study the influence of low temperature on the morphology of the products synthesized with other templates, several amines were employed to conduct the synthesis (the gel ratios for the syntheses are xR/0.5–0.8Al_2O_3/1.0P_2O_5/0.5SiO_2/50H_2O, 120 °C, 48 h). As can be seen in Fig. 6c, when dimethylethanolamine is used as the template, a squama-like superstructure of SAPO-5 is obtained, while a spindle-like morphology forms if hexamethyleneimine and choline chloride are added to the slurry as mixed structure-directing agents (Fig. 6d). Both samples show an aggregated morphology with growth inhibition along the *c*-axis. More interestingly, contrary to the above results, a hexagonal prism-like superstructure assembled by numerous thin rod-like crystals is obtained using tripropylamine as the template (Fig. 6e), indicating that the growth rate along the *c*-axis is much faster than that of the *a*-axis. Furthermore, when using TEAOH as the template, individual SAPO-5 nanosheets form instead of their aggregation. As a comparison, the above syntheses were also performed at 200 °C and the SEM images are presented in Fig. S2.† Obviously, the products synthesized at low temperature have different morphologies from their high-temperature counterparts. It implies that the crystal growth habit may be changed by varying the crystallization temperature, though the concrete growth behavior is template-dependent.

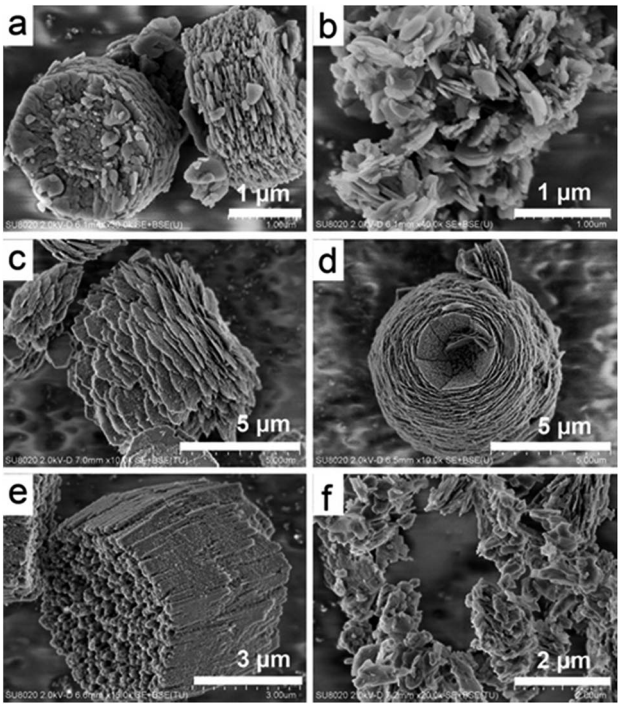

Fig. 6 SEM images of the samples prepared with different templates: (a) TEABr/TEA (x = 0.5/1.5, SAPO-5-NS2); (b) TEABr/TEA (x = 1.0/1.5); (c) dimethylethanolamine (x = 1.5); (d) hexamethyleneimine/choline chloride (x = 1.0/0.5); (e) TPA (x = 1.5); (f) TEAOH (x = 1.5).

Synthesis and characterization of MeAPO-5 nanosheet assemblies

Additionally, MeAPO-5s (Me = Co, Mn, and Cr) with nanosheet assembly morphology (designated as MeAPO-5-NS) were synthesized with a similar gel composition to that of SAPO-5-NS1 at 120 °C. The XRD patterns of the MeAPO-5-NS samples shown in Fig. S3† give characteristic peaks of AFI-type molecular sieves. The weak diffraction peak at 9.4° observed for CoAPO-5-NS implies the existence of a small amount of CHA molecular sieve. Fig. 7 shows the SEM images of the three samples. It could be seen that the structure of CrAPO-5-NS is quite similar to that of SAPO-5-NS1, but the stacked layers become less organized for CoAPO-5-NS and MnAPO-5-NS. This suggests that metals can exert an influence on the product morphology. Yu *et al.* have also reported that $AlPO_4$-5 crystals with inhibited growth along the [001] direction can be achieved by introducing the transition metals and polyethylene glycol.[59,60] The textual properties of the MeAPO-5-NS samples are given in Table 1. All the three samples show larger external surface areas and higher mesopore volumes than the conventional SAPO-5-C and MeAPO-5-C. The DR UV-Vis spectra of the three as-synthesized samples are presented in Fig. S5,† which are similar to those reported for the well-prepared metal-containing AlPO-5s,[61,62] suggesting the incorporation of the heteroatoms into the AFI framework.

Synthesis and characterization of CHA/AEI intergrowth CoAPO molecular sieves

In the present low-temperature synthesis system, an interesting result appeared when a small amount of Co instead of Si was introduced to the reaction gel with TEA and TEABr as the templates. The XRD pattern of the product is presented in Fig. 8. Clearly, a CHA/AEI intergrowth CoAPO zeolite (named as DNL-7-Co) was obtained from the system. Although a SAPO-type CHA/AEI intergrowth could be obtained when using TEA as the template,[63] this is the first report on the synthesis of CoAPO

Fig. 7 SEM images of CrAPO-5-NS (a), CoAPO-5-NS (b), and MnAPO-5-NS (c).

CHA/AEI intergrowth to the best of our knowledge. Though the presence of cobalt ions in the aluminophosphate gel with TEA as the template has been reported to favor the crystallization of CoAPO-34 over CoAPO-5,[64] herein, both cobalt ions and TEABr are inferred to be important for the formation of DNL-7-Co. Without the addition of TEABr, the CoAPO-5 nanosheet assembly would be obtained as the product. Besides, low temperature is also crucial for the formation of a CHA/AEI intergrowth structure. When increasing the crystallization temperature to 200 °C, pure CoAPO-5 was acquired from the same gel.

^{13}C MAS NMR was employed to investigate the incorporation of amines into the products (Fig. 9). The peak centred at *ca.* 8 ppm could be assigned to the $-CH_3$ group of TEA and TEA^+, while the $-CH_2-$ groups of TEA^+ and TEA give signals at 53.5 and 49 ppm, respectively. It is thus concluded that TEA and TEA^+ acted as co-templates for the formation of DNL-7-Co. The further peak deconvolution shows that the molar ratio of TEA^+/TEA in the product is much higher than that in the starting gel (3.1 *vs.* 0.5), suggesting that TEA^+ has a stronger structure directing ability to DNL-7-Co than TEA.

The SEM images of DNL-7-Co are shown in Fig. 8, which show spherical architectures of ~3 μm with a rather rough surface. Further magnification reveals that the spherical structure is composed of intercrossed nanosheets, which more closely resemble the platelet-like morphology of SAPO-18 with AEI topology.[65] Fig. 8c displays the DR UV-Vis spectrum of the as-synthesized DNL-7-Co, which presents an intense triplet band between 500 and 650 nm, characteristic of tetrahedrally coordinated Co^{2+} ions in the framework of molecular sieves.

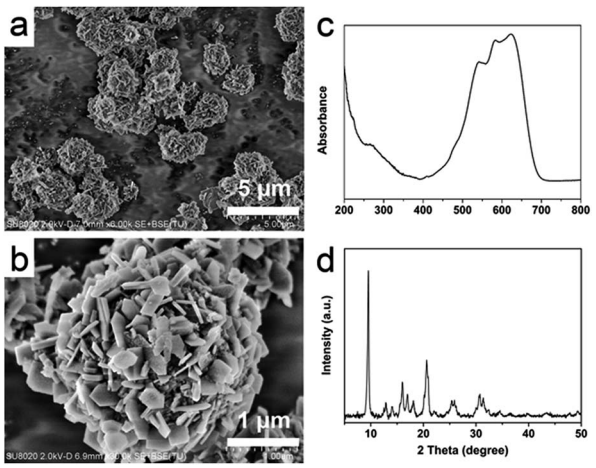

Fig. 8 (a and b) SEM images of DNL-7-Co at different magnifications; (c) DR UV-Vis spectrum of the as-synthesized DNL-7-Co; (d) XRD pattern.

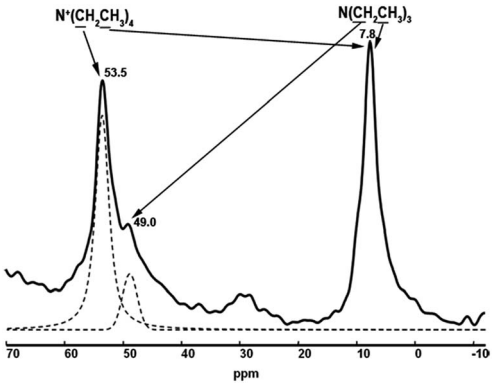

Fig. 9 ^{13}C MAS NMR spectrum of the as-synthesized DNL-7-Co.

The nitrogen sorption isotherms of DNL-7-Co (Fig. S6†) can be categorized as a type IV isotherm and the inset is the corresponding BJH pore size distribution curve. It is clear that the mesopore size distribution is not uniform and most of the pores fall into the size ranging from 20 to 30 nm. Considering the morphology of DNL-7-Co, the mesopores should arise from the spaces among the less ordered nanosheets. The calculated pore volume and surface area are listed in Table 1. It exhibits a BET surface area of 544 $m^2\ g^{-1}$ and a micropore volume of 0.23 $cm^3\ g^{-1}$, which are close to those of SAPO-18 and indicate the good crystallinity of DNL-7-Co.

Catalytic performance

Alkylation of benzene with benzyl alcohol. The short 12-membered ring channels parallel to the *c*-axis in the nanosheets of SAPO-5 assemblies make them promising solid acid catalysts. Herein, the space-requiring alkylation of benzene with benzyl alcohol was chosen as a model catalytic reaction to investigate the catalytic activity of the SAPO-5 nanosheet assembly. For comparison, the SAPO-5-C mentioned above was also tested under the same conditions. Despite the fact that NH_3-TPD curves (Fig. S7†) show that SAPO-5-NS2 possesses a lower acid concentration than SAPO-5-C, it exhibits superior catalytic activity to the latter (Fig. 10). After the reaction for 1 h, the conversion of benzyl alcohol readily achieves almost 100% over SAPO-5-NS2, while the mixtures with SAPO-5-C are far from the complete reaction (47.7% conversion). In addition, SAPO-5-NS2 gives a selectivity of 99.4% for the target product diphenylmethane, which is about 10% higher than SAPO-5-C. According to the textural and acidity properties of the two samples, the higher activity of SAPO-5-NS2 could result from its shorter diffusion path and larger external surface area.

Oxidation of cyclohexane with oxygen. Selective oxidation of cyclohexane is very attractive nowadays because its products are the intermediates for the manufacture of Nylon-6 and Nylon-6-6.[66] The commercial process for cyclohexane oxidation is carried out over soluble metal cobalt salt or metal-boric acid affording 4% conversion and 70–85% selectivity to cyclohexanone and cyclohexanol. However, owing to the limitations of

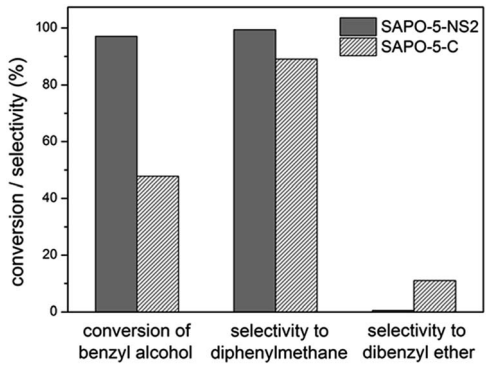

Fig. 10 A comparison of the catalytic performance of SAPO-5-NS2 and SAPO-5-C in the alkylation of benzene with the benzyl alcohol reaction. Reaction conditions: catalyst 031 g; benzene 29.8 g; benzyl alcohol 0.52 g; 160 °C; 1 h; N_2 3.4–3.6 MPa.

Table 2 The results of cyclohexane oxidation over MnAPO-5 catalysts

Sample	Me (wt%)	Conversion[a] (%)	Selectivity[b] (%)			
			ol	one	CHHP	Others
MnAPO-5-C	1.6	3.5	35.8	31.2	18.5	14.5
MnAPO-5-NS	1.7	6.9	47.6	32.0	7.3	13.1

[a] Conversion of cyclohexane; cyclohexane 23.5 mL, CHP 0.07 mL, cyclohexane/metal in catalyst = 2200 in mole, O_2 1.4 MPa, 130 °C, 3 h. [b] ol = cyclohexanol, one = cyclohexanone, CHHP = cyclohexyl hydroperoxide, and others = multifunction oxidation products from ring cleavage.

these soluble catalysts, in recent years, transition-metal-substituted molecular sieves have appeared to be promising heterogeneous and recyclable catalysts. In consideration of this, the oxidation of cyclohexane was investigated over the MnAPO-5-NS catalyst. Moreover, conventional MnAPO-5-C was tested as a reference catalyst. As shown in Table 2, the cyclohexane conversion catalyzed by MnAPO-5-NS (6.9%) is more than that over MnAPO-5-C (3.5%), which can be attributed to its structural and pore characteristics. The lower selectivity of CHHP (a hydroperoxide intermediate) over MnAPO-5-NS should also result from the ample contact of CHHP with the catalytic sites.

Conclusion

In this work, we have presented a facile one-pot hydrothermal strategy to fabricate hierarchical aluminophosphate-based molecular sieves without the help of surfactants by simply lowering the crystallization temperature. The SAPO-5-NS obtained is composed of oriented attached nanosheets with a thickness of 40–100 nm and it is revealed that the most exposed surface of the nanosheet is the {001} plane, which therefore reduced the diffusion length. Low crystallization temperature is proved to change the crystal growth habit with a growth inhabitation in the [001] direction and play a key role in the formation of the unique hierarchical structure. Based on the experimental results, a growth mechanism involving the assembly of the preformed nanosheets into the ordered superstructure is proposed, which more conforms to the non-classical crystallization mechanism. Furthermore, nanostructured SAPO-5 with different morphologies could be achieved at a low temperature (120 °C) upon variation of the template, showing the template dependence of the morphologies. Importantly, this simple route could be extended to the synthesis of metal-aluminophosphate molecular sieves and MeAPO-5s (Me = Co, Mn, and Cr) and a CHA/AEI intergrowth CoAPO could be obtained, all of which have an aggregated morphology constructed by nanosheets. Moreover, compared with the conventional samples, SAPO-5-NS2 and MnAPO-5-NS exhibit much better catalytic performance in the alkylation of benzene with benzyl alcohol and cyclohexane oxidation, respectively. This work offers a facile way to modify the crystal growth habit and construct hierarchical macrostructures with nanoscale zeolitic building units.

Notes and references

1 M. D. Ward, *Nature*, 2000, **405**, 293–294.
2 H. Cölfen and S. Mann, *Angew. Chem., Int. Ed.*, 2003, **42**, 2350–2365.
3 Z. Dai, A. Voigt, S. Leporatti, E. Donath, L. Dähne and H. Möhwald, *Adv. Mater.*, 2001, **13**, 1339–1342.
4 H. Li, Y. Jia, A. Wang, W. Cui, H. Ma, X. Feng and J. Li, *Chem.–Eur. J.*, 2014, **20**, 499–504.
5 H. Yao, H. Fang, X. Wang and S. Yu, *Chem. Soc. Rev.*, 2011, **40**, 3764–3785.
6 Z. Zhang, Y. Chen, S. He, J. Zhang, X. Xu, Y. Yang, F. Nosheen, F. Saleem, W. He and X. Wang, *Angew. Chem.*, 2014, **126**, 12725–12729.
7 Y. Wang, L. Zhu, X. Yang, E. Shao, X. Deng, N. Liu and M. Wu, *J. Mater. Chem. A*, 2015, **3**, 2934–2941.
8 Z. Qian, S. P. Hastings, C. Li, B. Edward, C. K. McGinn, N. Engheta and S. J. Park, *ACS Nano*, 2015, **9**, 1263–1270.
9 U. Simon, *Nat. Mater.*, 2013, **12**, 694–696.
10 W. Han and Z. Lin, *Angew. Chem., Int. Ed.*, 2012, **51**, 1534–1546.
11 K. Möller, B. Yilmaz, U. Müller and T. Bein, *Chem. Mater.*, 2011, **23**, 4301–4310.
12 M. Fukao, A. Sugawara, A. Shimojima, W. Fan, M. A. Arunagirinathan, M. Tsapatsis and T. Okubo, *J. Am. Chem. Soc.*, 2009, **131**, 16344–16345.
13 J. He, Y. Liu, T. Babu, Z. Wei and Z. Nie, *J. Am. Chem. Soc.*, 2012, **134**, 11342–11345.
14 Y. Guo, S. Harirchian-Saei, C. M. S. Izumi and M. G. Moffitt, *ACS Nano*, 2011, **5**, 3309–3318.
15 L. Emdadi, Y. Wu, G. Zhu, C.-C. Chang, W. Fan, T. Pham, R. F. Lobo and D. Liu, *Chem. Mater.*, 2014, **26**, 1345–1355.
16 X. Gong, *RSC Adv.*, 2014, **4**, 54494–54499.
17 X. Gong, *Phys. Chem. Chem. Phys.*, 2013, **15**, 10459–10465.
18 M. T. Reetz, M. Winter and B. Tesche, *Chem. Commun.*, 1997, 147–148.
19 C. Hamon, S. Novikov, L. Scarabelli, L. Basabe-Desmonts and L. M. Liz-Marzán, *ACS Nano*, 2014, **8**, 10694–10703.

20 Z. G. Estephan, Z. Qian, D. Lee, J. C. Crocker and S. J. Park, *Nano Lett.*, 2013, **13**, 4449–4455.
21 R. Yu, X. Wang, D. Wang, L. Ge, H. Shu and X. Yang, *J. Mater. Chem. A*, 2015, **3**, 3120–3129.
22 Y. Lin, X. Wang, G. Qian and J. J. Watkins, *Chem. Mater.*, 2014, **26**, 2128–2137.
23 X. Fei, W. Li, Z. Shao, S. Seeger, D. Zhao and X. Chen, *J. Am. Chem. Soc.*, 2014, **136**, 15781–15786.
24 L. Yang, Y. Zhu, H. Tong, Z. Liang and W. Wang, *Cryst. Growth Des.*, 2007, **7**, 2716–2719.
25 H.-K. Kim, S.-H. Park, S.-B. Yoon, C.-W. Lee, J. H. Jeong, K. C. Roh and K.-B. Kim, *Chem. Mater.*, 2014, **26**, 4838–4843.
26 X. Yang and E. D. Cranston, *Chem. Mater.*, 2014, **26**, 6016–6025.
27 A. Corma, *Chem. Rev.*, 1997, **97**, 2373–2420.
28 M. E. Davis, *Nature*, 2002, **417**, 813–821.
29 Z. L. Wang, *Adv. Mater.*, 1998, **10**, 13–30.
30 L. Gueudré, M. Milina, S. Mitchell and J. Pérez-Ramírez, *Adv. Funct. Mater.*, 2014, **24**, 209–219.
31 J. Song, L. Ren, C. Yin, Y. Ji, Z. Wu, J. Li and F.-S. Xiao, *J. Phys. Chem. C*, 2008, **112**, 8609–8613.
32 M. Antonietti, N. Fechler and T.-P. Fellinger, *Chem. Mater.*, 2013, **26**, 196–210.
33 T. Tang, L. Zhang, W. Fu, Y. Ma, J. Xu, J. Jiang, G. Fang and F.-S. Xiao, *J. Am. Chem. Soc.*, 2013, **135**, 11437–11440.
34 Y. Zhang, K. Zhu, X. Duan, X. Zhou and W. Yuan, *J. Mater. Chem. A*, 2014, **2**, 18666–18676.
35 M. Choi, H. S. Cho, R. Srivastava, C. Venkatesan, D.-H. Choi and R. Ryoo, *Nat. Mater.*, 2006, **5**, 718–723.
36 F. Xiao, L. Wang, C. Yin, K. Lin, Y. Di, J. Li, R. Xu, D. Su, R. Schlögl, T. Yokoi and T. Tatsumi, *Angew. Chem., Int. Ed.*, 2006, **45**, 3090–3093.
37 K. Na, C. Jo, J. Kim, K. Cho, J. Jung, Y. Seo, R. J. Messinger, B. F. Chmelka and R. Ryoo, *Science*, 2011, **333**, 328–332.
38 L. Chen, X. Li, J. C. Rooke, Y. Zhang, X. Yang, Y. Tang, F.-S. Xiao and B.-L. Su, *J. Mater. Chem.*, 2012, **22**, 17381–17403.
39 L. Ren, Q. Guo, H. Zhang, L. Zhu, C. Yang, L. Wang, X. Meng, Z. Feng, C. Li and F.-S. Xiao, *J. Mater. Chem.*, 2012, **22**, 6564–6567.
40 Y. Fang, H. Hu and G. Chen, *Chem. Mater.*, 2008, **20**, 1670–1672.
41 K. Möller, B. Yilmaz, R. M. Jacubinas, U. Müller and T. Bein, *J. Am. Chem. Soc.*, 2011, **133**, 5284–5295.
42 M. Choi, K. Na, J. Kim, Y. Sakamoto, O. Terasaki and R. Ryoo, *Nature*, 2009, **461**, 246–249.
43 J. Zhu, Y. Zhu, L. Zhu, M. Rigutto, A. van der Made, C. Yang, S. Pan, L. Wang, L. Zhu, Y. Jin, Q. Sun, Q. Wu, X. Meng, D. Zhang, Y. Han, J. Li, Y. Chu, A. Zheng, S. Qiu, X. Zheng and F.-S. Xiao, *J. Am. Chem. Soc.*, 2014, **136**, 2503–2510.
44 E.-P. Ng, D. Chateigner, T. Bein, V. Valtchev and S. Mintova, *Science*, 2012, **335**, 70–73.
45 P. Huang, J. Xu, C. Wang, F. Deng and W. Yan, *RSC Adv.*, 2014, **4**, 39011–39019.
46 B. Modhera, M. Chakraborty, P. A. Parikh and R. V. Jasra, *Cryst. Res. Technol.*, 2009, **44**, 379–385.
47 L. Tosheva and V. P. Valtchev, *Chem. Mater.*, 2005, **17**, 2494–2513.
48 V. P. Valtchev, L. Tosheva and K. N. Bozhilov, *Langmuir*, 2005, **21**, 10724–10729.
49 S. Tanahashi, T. Moteki and T. Okubo, *Chem. Lett.*, 2012, **41**, 889–891.
50 Z. Liu, T. Wakihara, D. Nishioka, K. Oshima, T. Takewaki and T. Okubo, *Chem. Mater.*, 2014, **26**, 2327–2331.
51 C. A. Fyfe, R. J. Darton, H. Mowatt and Z. S. Lin, *Microporous Mesoporous Mater.*, 2011, **144**, 57–66.
52 J. C. Groen, L. A. A. Peffer and J. Pérez-Ramírez, *Microporous Mesoporous Mater.*, 2003, **60**, 1–17.
53 T. Kodaira, K. Miyazawa, T. Ikeda and Y. Kiyozumi, *Microporous Mesoporous Mater.*, 1999, **29**, 329–337.
54 A. Iwasaki, T. Sano, T. Kodaira and Y. Kiyozumi, *Microporous Mesoporous Mater.*, 2003, **64**, 145–153.
55 S. H. Jhung, J.-S. Chang, Y. K. Hwang and S.-E. Park, *J. Mater. Chem.*, 2004, **14**, 280–285.
56 H. Cöelfen and M. Antonietti, *Mesocrystals and Nonclassical Crystallization*, John Wiley & Sons, 2008.
57 F. Li, L. Yang, G. Xu, X. Huang, X. Yang, X. Wei, Z. Ren, G. Shen and G. Han, *J. Alloys Compd.*, 2013, **577**, 663–668.
58 K. E. Jelfs, B. Slater, D. W. Lewis and D. J. Willock, *Stud. Surf. Sci. Catal.*, 2007, **170B**, 1685–1692.
59 X. Cao, J. Yu and R. Xu, *Chem. Mater.*, 2008, **20**, 2160–2164.
60 D. Tian, W. Yan, Z. Wang, Y. Wang, Z. Li, J. Yu and R. Xu, *Cryst. Growth Des.*, 2009, **9**, 1411–1414.
61 A. A. Verberckmoes, B. M. Weckhuysen and R. A. Schoonheydt, *Microporous Mesoporous Mater.*, 1998, **22**, 165–178.
62 N. Rajić, D. Stojaković, S. Hoçevar and V. Kaučič, *Zeolites*, 1993, **13**, 384–387.
63 Y. Li, Y. Huang, J. Guo, M. Zhang, D. Wang, F. Wei and Y. Wang, *Catal. Today*, 2014, **233**, 2–7.
64 M. G. Uytterhoeven and R. A. Schoonheydt, *Microporous Mater.*, 1994, **3**, 265–279.
65 R. Wendelbo, D. Akporiaye, A. Andersen, I. M. Dahl and H. B. Mostad, *Appl. Catal., A*, 1996, **142**, L197–L207.
66 G. Sankar, R. Raja and J. Thomas, *Catal. Lett.*, 1998, **55**, 15–23.